Automatic Auroral Boundary Determination Algorithm with Deep Feature and Dual Level Set

ZeMing Zhou[1], ChenJing Tian[1], HuaDong Du[1], PingLv Yang[1], Xiaofeng Zhao[1], and Su Zhou[2]

[1]National University of Defense and Technology
[2]Guiyang University

November 21, 2022

Abstract

The morphology of the auroral oval is an important geophysical parameter that can be used to uncover the solar wind-geomagnetic field interaction process and the intrinsic mechanism. However, it is still a challenging task to automatically obtain auroral poleward and equatorward boundaries completely and accurately. In this paper, a new model based on the deep feature and dual level set method is proposed to extract the auroral oval boundaries in the images acquired by the Ultraviolet Imager (UVI) onboard the Polar spacecraft. With the deep feature extracted by the convolutional neural network (CNN), the corresponding deep feature energy functional is constructed and incorporated into the variational segmentation framework. The dual level set method is implemented to extract the accurate poleward and equatorward boundaries with the gradient descent flow. The experimental results on the test data set demonstrate that this model can extract complete auroral oval contours that are consistent well with expert annotations and owns higher accuracy compared with the previously proposed methods. Besides, the comparison between the extracted auroral boundaries and the precipitating boundaries determined by Defense Meteorological Satellite Program (DMSP) SSJ precipitating particle data validates that the proposed method is trustworthy to capture the global morphology of the auroral ovals.

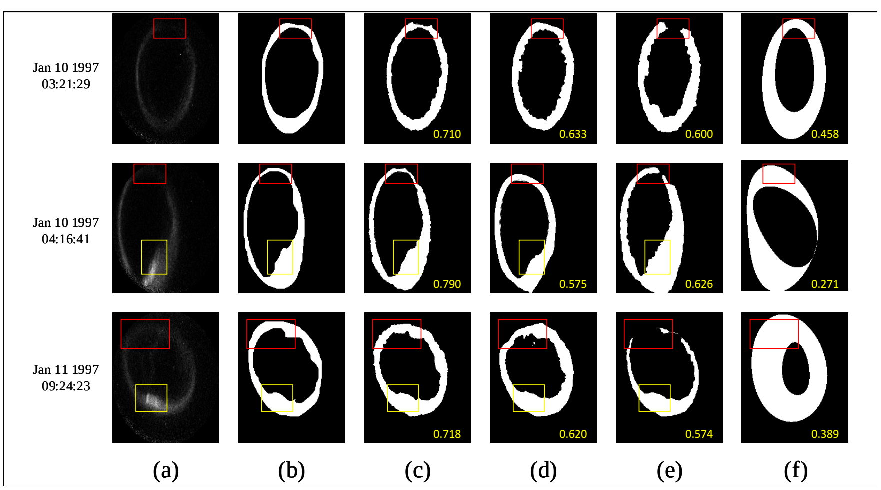

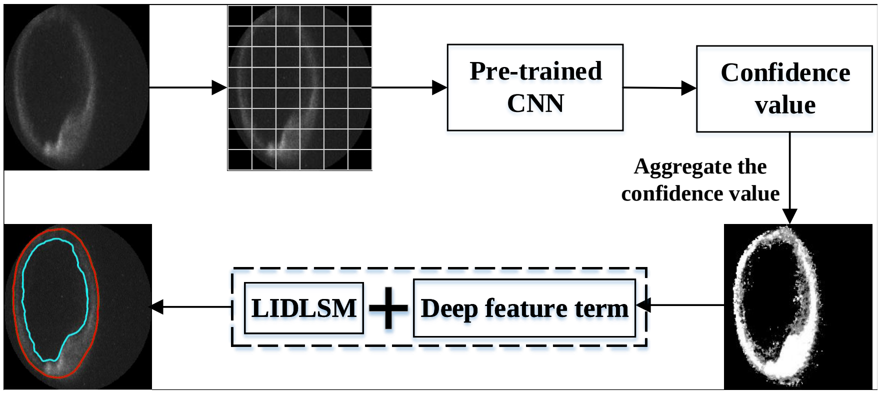
Pre-trained CNN
Confidence value
Aggregate the confidence value
LIDLSM
Deep feature term

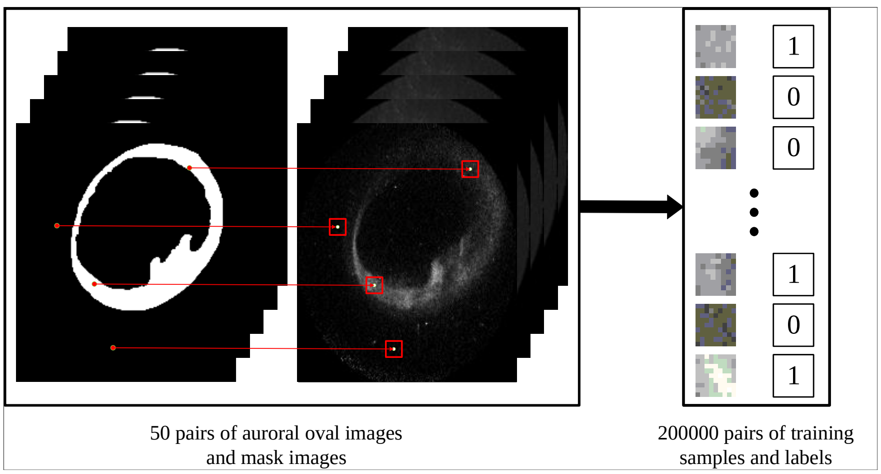
1
0
0
1
0
1
50 pairs of auroral oval images and mask images
200000 pairs of training samples and labels

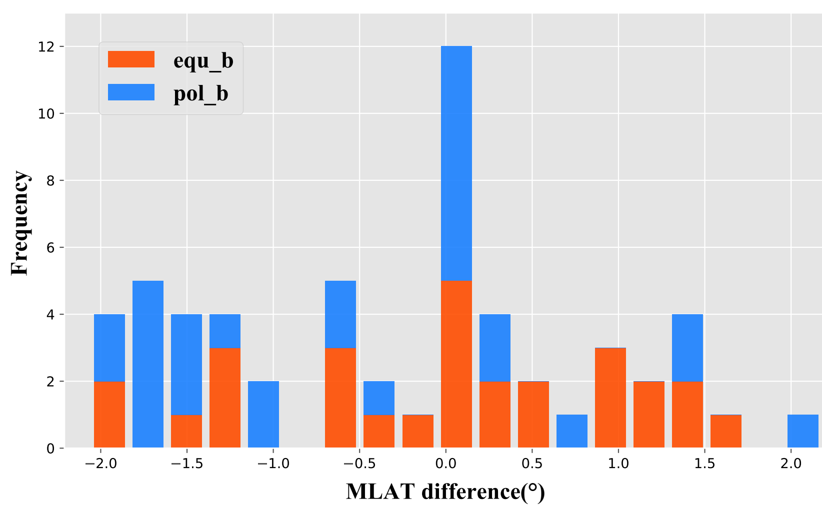
equ_b
pol_b
Frequency
MLAT difference(°)
0
2
4
6
8
10
12
−2.0
−1.5
−1.0
−0.5
0.0
0.5
1.0
1.5
2.0

Automatic Auroral Boundary Determination Algorithm with Deep Feature and Dual Level Set

Chen-Jing Tian[1], Hua-Dong Du[1], Ping-Lv Yang[1], Ze-Ming Zhou[1], Xiao-Feng Zhao[1], and Su Zhou[2]

[1]Institute of Meteorology and Oceanology, National University of Defense Technology, Nanjing, China. [2]School of Electronic and Communication Engineering, Guiyang University, Guiyang, China.

Corresponding author: Ze-Ming Zhou[1] (zhou_zeming@nudt.edu.cn)

Su Zhou[2] (zhousujob@gmail.com)

Key Points:

- We adopt the convolutional neural network to extract the deep features from Polar/UVI auroral images
- The deep feature energy functional is constructed and incorporated into the variational framework to determine the auroral boundaries
- The extracted boundaries agree well with expert annotations and conform to the DMSP precipitating particle data

Abstract

The morphology of the auroral oval is an important geophysical parameter that can be used to uncover the solar wind-geomagnetic field interaction process and the intrinsic mechanism. However, it is still a challenging task to automatically obtain auroral poleward and equatorward boundaries completely and accurately. In this paper, a new model based on the deep feature and dual level set method is proposed to extract the auroral oval boundaries in the images acquired by the Ultraviolet Imager (UVI) onboard the Polar spacecraft. With the deep feature extracted by the convolutional neural network (CNN), the corresponding deep feature energy functional is constructed and incorporated into the variational segmentation framework. The dual level set method is implemented to extract the accurate poleward and equatorward boundaries with the gradient descent flow. The experimental results on the test data set demonstrate that this model can extract complete auroral oval contours that are consistent well with expert annotations and owns higher accuracy compared with the previously proposed methods. Besides, the comparison between the extracted auroral boundaries and the precipitating boundaries determined by Defense Meteorological Satellite Program (DMSP) SSJ precipitating particle data validates that the proposed method is trustworthy to capture the global morphology of the auroral ovals.

1 Introduction

The Earth's auroral emissions are the results of collisions with the neutral constituents in the ionosphere of the precipitating charged particles from the solar wind (Boudouridis et al., 2003; Kvammen et al., 2019; Qian et al., 2011). In the observation of ground-based and satellite-borne imager instruments, the aurorae are roughly circular belts located around the geomagnetic poles, and also known as auroral ovals (Akasofu, 1965; Hu et al., 2017; Qian et al., 2011). The equatorward and poleward boundaries of auroral oval are important geophysical parameters that reflect the high latitude solar wind-magnetosphere-ionosphere coupling process and provide clues to uncover the physical mechanism for space weather prediction (Q. Yang et al., 2019). The exact morphology and position of the equatorward boundary rely on the precipitated energetic particles and the magnetospheric electromagnetic field. The poleward boundary is believed to be the open-closed field line boundary, which is most frequently influenced by the solar wind condition. (Kauristie et al., 1999). When the interplanetary magnetic field (IMF) is southward, it will reconnect with the geomagnetic field, which points northward. The reconnection on the dayside magnetopause would produce open field lines which are dragged by the solar wind into the magnetotail. Soon afterward, the reconnection in the magnetotail leads to the closure of the magnetic open flux, which releases the stored magnetotail energy and causes the contraction of polar cap region. (Boudouridis et al., 2005; Hoshi et al., 2018). It is noted that accurately obtaining the overall shape and variations of the auroral oval is important to investigate the interaction between the solar wind, the magnetosphere, and the ionosphere (Ding et al., 2017).

Auroral boundaries can mainly be defined via three observation methods, including all-sky imagers, satellite imagers, and precipitating particle detectors. Since the in-situ particle detector measures precipitating particles along the spacecraft track, it only obtains the boundary of the auroral oval at one point instead of a glob view. Compared with the in-situ observations, the imagers onboard spacecrafts can provide observations for the global morphology of auroral oval (Carbary & J., 2003).

Many researchers have attempted to delineate auroral boundaries automatically from the auroral images captured by satellite imagers, in which the auroral oval images taken by Ultraviolet Imager (UVI) onboard the Polar satellite have been widely studied. Automatic auroral boundaries determination from the UVI images has utilized many techniques from computer vision and pattern recognition. For example, Cao et al. presented the linear least-squares based randomized Hough transform (LLS-RHT) (Cao & Newman, 2009), with the help of prior shape knowledge, to obtain the complete auroral oval boundaries. Assuming the outer contour is similar to ellipse, Liu et al. applied k-means, elliptical fitting, and maximal similarity-based region merging (MSRM) for auroral boundaries extraction (Liu et al., 2013). Ding et al. proposed the algorithm based on fuzzy local information C-means (FCM) clustering and quasi-elliptical fitting (QEF) to determine the auroral boundaries in merged images which combined the auroral oval images from Thermosphere-Ionosphere-Mesosphere Energetics and Dynamics (TIMED) satellite and Defense Meteorological Satellite Program (DMSP) (Ding et al., 2017).

Since the active contour model (ACM) was proposed by Kass et al. (1988), it has been widely pursued and employed to image segmentation. The principal idea of the ACM is that, driving by the gradient descent flow of the energy function, the deformation curve will evolve constantly and finally dock at the boundary of the interested object (Sun et al., 2018). The morphology of auroral oval varies rapidly over time; therefore, it is very suitable to adopt ACM for the determination of the auroral boundaries in UVI images. Yang et al. proposed the shape-initialized and intensity-adaptive level set method (SIIALSM) to obtain the auroral morphologies (X. Yang et al., 2014a; X. Yang et al., 2014b). Shi et al. inserted the interval type-2 fuzzy sets (IT2FS) into the ACM to improve the boundary extraction model's performance (Shi et al., 2017). Yang et al. incorporated the auroral oval's shape feature into the local information based dual level set method (LIDLSM) to extract auroral boundaries in UVI images (P. Yang et al., 2017).

With the widespread application of ground-based optical all-sky imagers (ASI), millions of ASI images are captured annually. Thus, many methods are applied to extract local aurora boundaries, which help to study the near-Earth space physical processes for geosciences (Clausen & Nickisch, 2018). To generate more training images captured by ASI, Niu et al. adopted the affine transformation and mask-region convolutional neural network (mask-RCNN) to detect the auroral arc for the assessment of the auroral arc width (Niu et al., 2019). Yang et al. applied the simplified cycle-consistent generative adversarial network to extract the key local structures from ASI images (Q. Yang et al., 2019).

With the advancement of deep-learning techniques, especially of the convolutional neural network (CNN), many groundbreaking results have been obtained in the last few years (Ham et al., 2019; Silver et al., 2017). As the most commonly used network, CNN has gained great popularity in computer vision tasks (Girshick, 2015; Goodfellow et al., 2014; Zhao et al., 2017). In this work, CNN is employed to extract the deep feature in UVI images, which is represented by the confidence values that pixels locate in the oval zone. Those confidence values are then utilized to construct the deep feature energy term, which is incorporated into the energy functional of LIDLSM. By minimizing the total energy functional, the auroral oval boundaries can be obtained eventually. The experiments on the test data set demonstrate that the proposed model can identify auroral oval boundaries with higher accuracy.

The procedure of our algorithm is shown in Figure 1. The first step is to train the CNN on the training data set. The second step is to construct the deep feature energy term with the confidence value extracted by pre-trained CNN. Finally, the deep feature energy term is worked with LIDLSM for the determination of auroral oval boundaries.

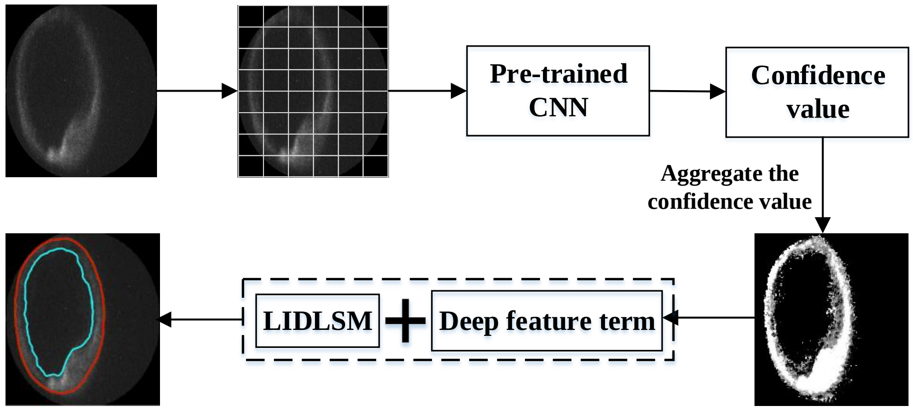

Figure 1. Overview of the proposed auroral oval boundaries determination method.

2 Data Sets

2.1 The UVI Data Set

The auroral images used in this study are derived from the UVI instrument onboard Polar spacecraft (Torr et al., 1995), which has been operating by National Aeronautics and Space Administration (NASA) since February 1996. As a satellite belonging to the Global Geospace Science (GGS) portion of the International Solar-Terrestrial Physics (ISTP) program (Hoffman & Hesse, 1996), Polar was launched into an 86° inclination orbit with 2×9 R_E and a period of ~18 hours (Carbary & J., 2003; Hoffman & Hesse, 1996). The auroral oval images are obtained by the UVI in the Lyman-Birge-Hopfield long (LBHL, 160-180 nm) band emissions. (Hu et al., 2017). The LBHL emissions are produced by N_2 (Nitrogen molecules) and usually caused by precipitating electrons at an altitude of around 120 km (Brittnacher et al., 1997). The image frame has 228×200 pixels, and a single pixel corresponds to a 40×40 km spatial resolution at an altitude of 100 km looking from the spacecraft apogee.

The auroral images in the UVI data set were taken by Polar UVI imager on Jan 1, 1997, Jan 4, 1997, Jan 10, 1997, Jan 11, 1997, Jan 15, 1998, Jan 25, 1998, and Jan 27, 1998. All of these images have complete oval contours and are collected in the winter of the northern hemisphere, and thus auroral LBHL emissions are not influenced by dayglow. Among the UVI images, 50 images captured on Jan 1, 1997, are utilized to obtain the CNN training samples, and the remaining 300 images are employed to validate the performance of the proposed algorithm. The UVI data set also contains the auroral boundary images, which were annotated and cross-verified by two experts (Meng et al., 2019; P. Yang et al., 2017). In addition, the corresponding mask images are included based on the annotated boundary image to mark the auroral oval region with white color, and the background region with black color. A set of corresponding UVI auroral image, annotated boundary image, and mask image are shown in Figure 2.

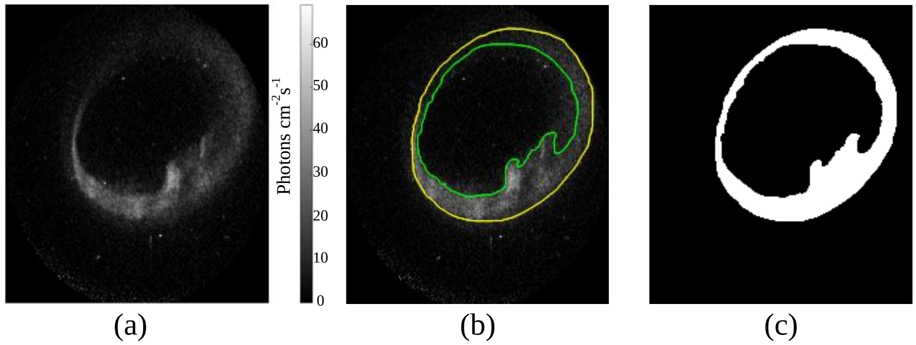

Figure 2. UVI data set images: (a) the auroral image captured at Jan 1, 1997, 02:28:43; (b) the annotated auroral boundary image; (c) the corresponding mask image.

2.2 The DMSP Data Set

The U.S. Air Force has been operating the Defense Meteorological Satellite Program (DMSP) spacecraft since 1965. These spacecrafts are Sun-synchronous, polar-orbiting with an orbital period of 101 min, an inclination of 98.9°, and an altitude of 840 km (Schumaker et al., 1988). The Special Sensor J/4 (SSJ/4) onboard DMSP F6-F15 spacecraft measures the energy fluxes of precipitating electrons and ions in the energy range between 30 eV and 30 keV (Redmon et al., 2017). Utilizing the particle precipitating data observed by the DMSP/SSJ detector, Newell et al. introduced a set of operational algorithms to identify the auroral precipitation boundaries (Ding et al., 2017; Newell et al., 1996). Since the auroral radiance captured by the UVI is considered to be proportional to the energy flux of precipitating electrons, the precipitation boundaries b1e and b5e determined by the SSJ/4 precipitating electrons in the nightside are suitable to compare with the extracted auroral boundaries from UVI images. The particle boundaries b1i, b2e, b2i, b5i, and b6 are also assembled for comparison in Section 4. As reported by the definitions in (Newell et al., 1996), B1e and b1i indicate the "zero-energy" convection boundaries for electrons and ions, respectively. B2e and b2i are the points where the electron or ion energy flux is neither increasing or decreasing. B5e and b5i correspond to the poleward boundaries of the main auroral oval with the electron or ion energy flux drop by a factor of at least four over ~0.2° latitude range. B6 is the poleward boundary of the subvisual drizzle roughly adjacent to the oval (Newell et al., 1996).

3 Algorithm Description

3.1 The Retrospect of LIDLSM

In LIDLSM, Yang et al. took advantage of dual level set to extract the poleward and equatorward boundaries of the auroral oval (P. Yang et al., 2017). Suppose that $\Omega \subset R^2$ is an image domain. $I(u): \Omega \to R$ represents the grayscale image, in which $u \subset \Omega$. ϕ_1 and ϕ_2 represent the inner and outer level set, respectively. The proposed energy functional of LIDLSM method is defined as:

$$E(\phi_1,\phi_2) = \lambda \int_{\Omega} \frac{(|\phi_1(u)-\phi_2(u)|-\mu)^2}{2\sigma^2} du + \beta \sum_{i=1}^{2} \int_{\Omega} |\nabla H(\phi_i(u))| \, du + \sum_{i=1}^{2} \int_{\Omega} \delta(\phi_i(u)) \int_{O} H(\phi_i(v))(I(v)-v_{inner})^2 + (1-H(\phi_i(v)))(I(v)-v_{outer})^2 \, dv du \quad (1)$$

in which the first term is the shape energy functional to prevent the interleave of two evolving curves represented by ϕ_1 and ϕ_2. It is assumed that the distance between ϕ_1 and ϕ_2 follows the Gaussian distribution (Meng et al., 2019; Woo et al., 2013). μ is the mean width between ϕ_1 and ϕ_2; σ is the standard deviation of the width. The second term is the regularization energy functional to guarantee the numerical computation stability; $H(\cdot)$ is the Heaviside function. The third term refers to the local information energy functional to drive the deformation curve evolving to the boundaries, in which $\mathrm{O} = \{v \mid \|v-u\| < r\}$ specifies the local window with a radius r centered on the point u. v_{inner} and v_{outer} indicate the localized mean intensity in $\{v \mid \phi_i(v) > 0,\ v \subset \mathrm{O}\}$ and $\{v \mid \phi_i(v) \le 0,\ v \subset \mathrm{O}\}$, respectively. $\delta(\cdot)$ is the Dirac function. λ and β are weight coefficients to trade-off the effects of different energy terms.

As shown in the white rectangle in Figure 3a, it is worth noting that, in the locally low-contrast regions of UVI images, the grayscales of the oval are similar to the background. LIDLSM can obtain complete boundaries of the aurora oval (Meng et al., 2019), but owns relatively low accuracy in those regions, as seen in Figure 3b. The boundaries obtained by LIDLSM deviated obviously from the annotated contours in Figure 3c. To remedy this defect of LIDLSM, in this paper, CNN is utilized to capture the subtle grayscale difference in the low-contrast regions, and with the aid of the CNN-based deep feature energy term, the deformation curve can evolve to the accurate boundaries of the auroral oval.

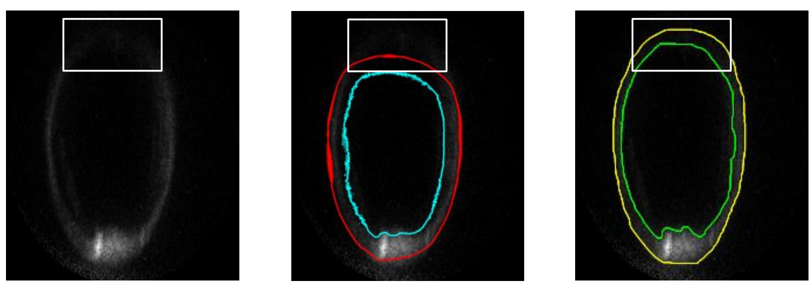

(a) (b) (c)

Figure 3. UVI image and extracted boundaries. (a) The UVI image captured at Jan 10, 1997, 03:40:12. (b) Extracted boundaries by LIDLSM. (c) Annotated boundaries by experts.

3.2 Training of CNN

As above-mentioned, 50 UVI images captured on Jan 1, 1997, and corresponding mask images are utilized to obtain the training samples and labels for CNN, respectively. The training samples extraction procedure is shown in Figure 4. 2000 auroral oval pixels and 2000 background pixels (red point) are selected randomly from each mask image (Tian et al., 2020). Centering the corresponding pixels (white point) in the UVI images, sub-images with the size of 11×11 are cropped and served as the training samples. The label of each training sample is the corresponding pixel's value in the mask image, that is, the value is 1 when the red point is in the auroral region; otherwise, the value is 0. As a result, 200000 pairs of training samples and labels are collected for training CNN.

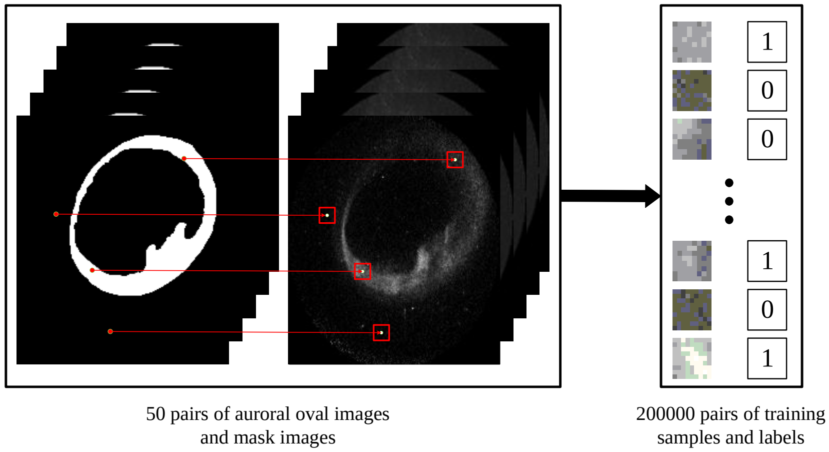

Figure 4. The extraction procedure of training samples and labels.

Owing to the advancement of CNNs, the accuracy of image classification has been greatly improved. CNNs usually include feature extraction unit and classification unit. The former starts with an input layer, which receives an input image with a fixed size. Subsequently, the input image is convolved with multiple learned kernels in the convolutional layers and output the results known as the feature map. In the classification unit, the feature map is flattened into a vector, which is processed in the fully-connected layers. Finally, the network outputs a confidence value from 0 to 1, which represents the probability that the input image belongs to a certain category (Phung & Rhee, 2019).

Inspired by (Kim et al., 2019), the CNN designed and used in our work includes four convolutional layers (Conv1-4) and three fully-connected layers (Full5-7). Table 1 lists the detailed operations used in the designed CNN. The “Filter size” defines the number of convolutional filters and receptive fields as “num × size × size.” The “Stride” specifies the convolution stride, which controls the shifting unit of the receptive field at one time. The “Padding” gives the spatial padding; in the proposed CNN, zeros are padded before each convolution to preserve the edge pixels’ information. The activation function in our work is the Rectification Linear Unit (RELU) (Nair & Hinton, 2010), which has the characteristics of simple calculation and stable gradient value. The “Dropout” techniques (Srivastava et al., 2014) are applied to the fully connected layers to prevent CNN from overfitting. The “Softmax” classifier (Fei & Zhang, 2011) is adopted in the last layer to output the confidence values that the center pixel of the sub-image patch belongs to the auroral and background regions, respectively.

The proposed CNN employed the cross-entropy loss function (de Boer et al., 2005) to optimize the network parameters:

$$Loss = -[y \log \hat{y} + (1-y)\log(1-\hat{y})] \tag{2}$$

in which y indicates the sample label, and $\hat{y}$ is the confidence value that the pixel belongs to the auroral oval region. In our experiments, the prediction accuracy reaches 93.7% after 30000 training epochs. Utilizing the pre-trained CNN, the confidence value can be extracted to show the probability that each pixel belongs to the auroral region.

Table 1. *CNN architecture.*

No.	Layer	Output Size	Filter Size	Stride	Padding	Dropout
1.	Input	11×11×1	-	-	-	-
2.	Conv1	11×11×32	32×3×3	1	1	-
3.	Relu	11×11×32	-	-	-	-
4.	Conv2	11×11×32	64×3×3	1	1	-
5.	Relu	11×11×64	-	-	-	-
6.	Conv3	11×11×32	32×3×3	1	1	-
7.	Relu	11×11×32	-	-	-	-
8.	Conv4	11×11×32	32×3×3	1	1	-
9.	Relu	11×11×32	-	-	-	-
10.	Flatten	1×1×1936	-	-	-	-
11.	Full5	1×1×1936	-	-	-	-
12.	Relu	1×1×1936	-	-	-	-
13.	Dropout	1×1×1936	-	-	-	0.25
14.	Full6	1×1×128	-	-	-	-
15.	Relu	1×1×128	-	-	-	-
16.	Dropout	1×1×128	-	-	-	0.5
17.	Full7	1×1×2	-	-	-	-
18.	Softmax	1×1×2	-	-	-	-

3.3 Definition of Deep Feature Energy Term

Inspired by the sliding window technique (Drożdż & Kryjak, 2017), we gather the sub-images (11×11) centered on each pixel in the test UVI images, which have a fixed frame of 228×200 pixels. Therefore, 45600 sub-images can be gathered from each image after padding zeros at the border. Input those sub-images into the pre-trained CNN; we can get the confidence value $\hat{y}$ for every pixel in the UVI images. It is assumed that $\hat{y} > 0.5$ in the auroral oval region, and $\hat{y} \le 0.5$ in the background region. The confidence map is the visualization of the confidence value $\hat{y}$, whose grayscale value of each pixel is $\hat{y}\times 255$. Figure 5 shows the UVI image and the corresponding confidence map. It is a challenging task to determine the auroral boundaries in the low-contrast region marked with the white rectangle in Figure 5a, which is in the same position as the white rectangle in Figure 3a. However, the proposed CNN still obtains the rough boundaries in that region, as depicted in Figure. 5b.

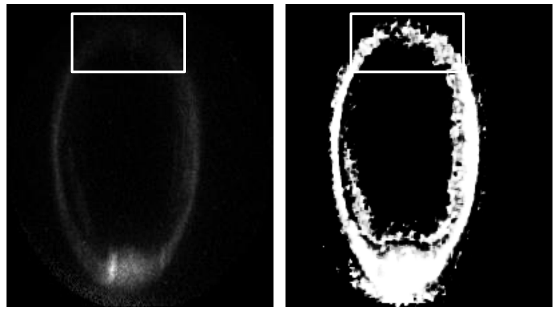

(a) (b)

Figure 5. Comparison of UVI image and corresponding confidence map. (a) UVI image captured at Jan 10, 1997, 03:40:12. (b). Corresponding confidence map.

Based on the confidence map, the deep feature energy term is proposed as follows:

$$E_{df} = \sum_{i=1}^{2} \int_{\Omega} (-1)^{i+1} v_{df} H(\phi_i(u)) du \tag{3}$$

in which $v_{df} = \hat{y} - 0.5$. According to the previous assumption, $v_{df} > 0$ in the auroral oval region, and $v_{df} \leq 0$ in the background region. Therefore, the deep feature energy term can reach the minimum when the deformation curves evolve to the confidence map determined boundaries. Ideally, if there is no prediction error of CNN, driven by the deep feature energy functional, the level set curves can evolve to the annotated boundaries exactly.

3.4 Implementation of The Proposed Model

In real situations, because of CNN classification error, the evolving curve can only advance to the nearby region of auroral oval boundaries. Therefore, in our work, the deep feature energy term is introduced into LIDLSM for more accurate boundaries determination. The total energy functional of our model is defined as:

$$\begin{aligned} E = {} & \lambda \int_{\Omega} \frac{(|\phi_1(u) - \phi_2(u)| - \mu)^2}{2\sigma^2} du + \beta \sum_{i=1}^{2} \int_{\Omega} |\nabla H(\phi_i(u))| \, du + \gamma \sum_{i=1}^{2} \int_{\Omega} (-1)^{i+1} v_{df} H(\phi_i(u)) du \\ & + \sum_{i=1}^{2} \int_{\Omega} \delta(\phi_i(u)) \int_{O} H(\phi_i(v))(I(v) - v_{inner})^2 + (1 - H(\phi_i(v)))(I(v) - v_{outer})^2 \, dv du \end{aligned} \tag{4}$$

As aforementioned, ϕ_1 and ϕ_2 are the inner and outer level set, respectively. O is a local window with radius r centered at u. Besides, λ, β and γ are weight coefficients, which are determined empirically to trade-off the effects of different energy terms.

By calculating the Gateaux derivative of the functional and introducing the time variable t, the gradient descent flow of ϕ_1 and ϕ_2 can be formulated as:

$$\begin{aligned} \frac{\partial \phi_1(u)}{\partial t} = {} & \lambda \frac{(|\phi_1(u) - \phi_2(u)| - \mu)}{\sigma^2} + \beta \delta(\phi_1(u)) div\left(\frac{\nabla \phi_1(u)}{|\phi_1(u)|}\right) - \gamma \delta(\phi_1(u)) v_{df} \\ & + \delta(\phi_1(u)) \int_{O} \delta(\phi_1(v))((I(v) - v_{inner})^2 - (I(v) - v_{outer})^2) dv \end{aligned} \tag{5}$$

$$\frac{\partial \phi_2(u)}{\partial t} = \lambda \frac{(|\phi_1(u) - \phi_2(u)| - \mu)}{\sigma^2} + \beta\delta(\phi_2(u)) div(\frac{\nabla \phi_2(u)}{|\phi_2(u)|}) + \gamma\delta(\phi_2(u)) v_{df} + \delta(\phi_2(u)) \int_{\Omega} \delta(\phi_2(v))((I(v) - v_{inner})^2 - (I(v) - v_{outer})^2) dv \quad (6)$$

The evolution equation can be discretized as:

$$\phi_i^{k+1}(u) = \phi_i^k(u) + \Delta t \frac{\partial \phi_i^k(u)}{\partial t} \quad (7)$$

in which k refers to k-th evolution. With the evolution of ϕ_1 and ϕ_2, the auroral boundaries are eventually determined. As shown in Figure 6, in comparison with the segmentation result of LIDLSM in Figure 6c, our method attained more accurate poleward and equatorward boundaries in the low-contrast regions marked by the white rectangle.

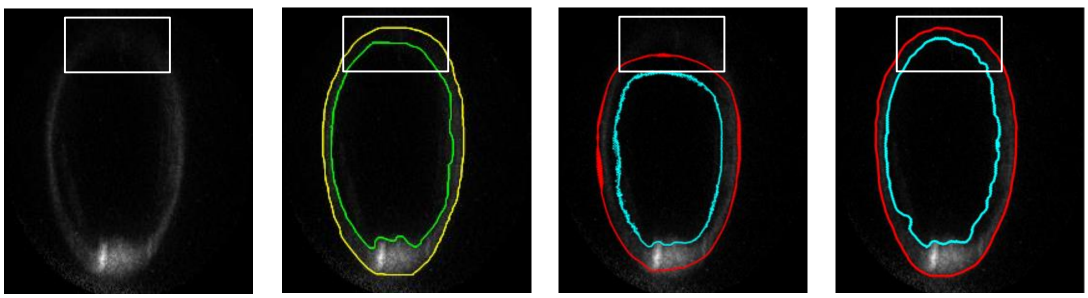

(a) (b) (c) (d)

Figure 6. Segmentation result of our method. (a) Auroral oval image captured at Jan 10, 1997, 03:40:12. (b) Annotated boundaries by experts. (c) Extracted boundaries by LIDLSM. (d) Extracted boundaries by the proposed method.

4 Experiment and Results

In order to validate the performance of the proposed algorithm, the experiment on the test data set is conducted to extract the auroral boundaries automatically. In the evaluation part, we compare the extracted boundaries with the annotated boundaries and the results obtained from three state-of-the-art methods, which include SIIALSM (X. Yang et al., 2014a), LIDLSM (P. Yang et al., 2017), FCM + QEF (Ding et al., 2017). Besides, the extracted boundaries are also compared with the boundary points identified by the DMSP SSJ/4 particle detector. In the experiments, the weight coefficients used in our experiment set empirically: λ=1.2, β=2, γ=1.3.

4.1 Visual Inspection and Metrics Evaluation

We picked up three UVI images that are challenging to extract boundaries for visual inspection; the results of different methods and the mask images are shown in Figure 7. Red rectangles mark the low-contrast regions in the UVI images, and yellow rectangles highlight the local details of the poleward boundaries. As for the first UVI image, the proposed method, LIDLSM, and FCM+QEF algorithm obtain the complete auroral boundaries, in which the results of LIDLSM and the proposed method are more consistent with the mask image in the low-contrast region. For the second and third UVI images, the proposed method, LIDLSM, and FCM+QEF algorithm also attain the complete auroral boundaries. However, the boundaries extracted by LIDLSM and FCM+QEF deviate significantly from those of the mask images.

Besides, for the second and third UVI images, the proposed method matches best in terms of the details marked by the yellow rectangle. The yellow values in Figure 7c-f give the intersection-over-union (IoU) index between the mask images and the results obtained by different methods. The IoU index is calculated as:

$$\text{IoU} = \frac{\text{Area of overlap}}{\text{Area of union}} = \frac{A_{seg} \cap A_{mask}}{A_{seg} \cup A_{mask}} \qquad (8)$$

where A_{seg} represents the auroral region determined by poleward and equatorward boundaries of each method, A_{mask} indicates that the auroral region in mask images. As reflected by the highest IoU values, the segmentation results of the proposed algorithm are consistent well with the expert annotations.

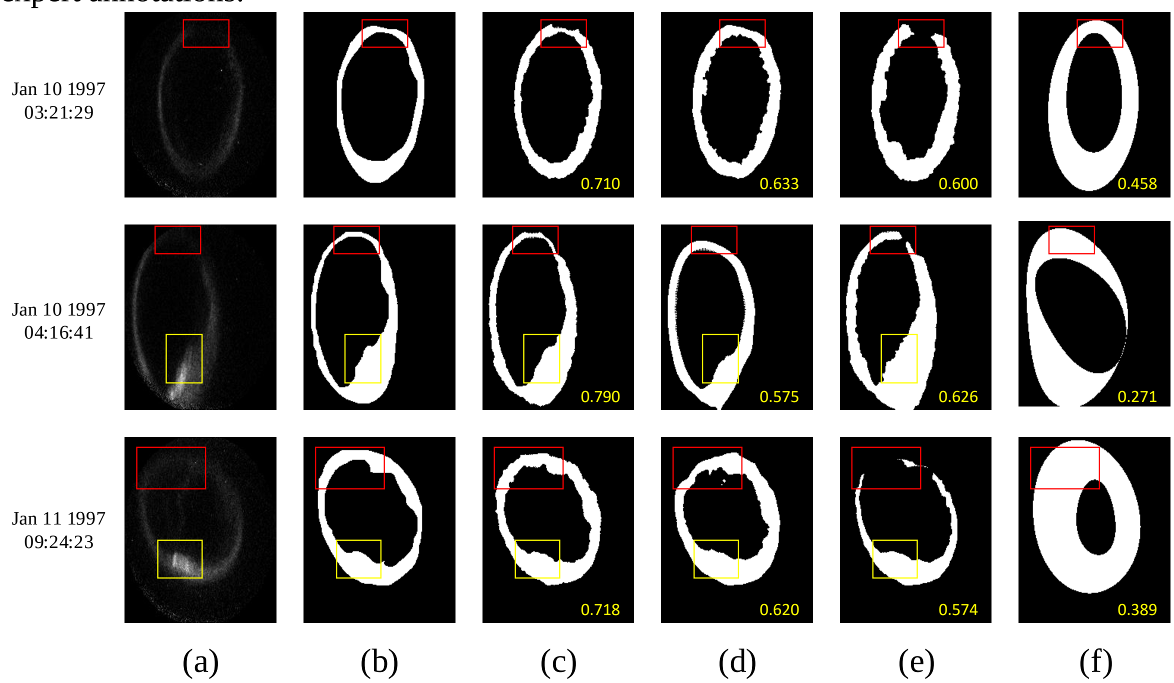

Figure 7. The UVI images, the mask images, and the auroral oval region extracted by different methods. (a) The UVI images. (b) The mask images. (c) The extracted auroral oval region of the proposed method. (d) The extracted auroral oval region of LIDLSM. (e) The extracted auroral oval region of SIIALSM. (f) The extracted auroral oval region of the FCM+QEF algorithm.

In addition to visual inspection, the accuracy of extracted boundaries is evaluated with four metrics, including *pixel deviation* (P_d), *percentage of gap pixels* (P_g), *percentage of distant pixels* (P_f), and *percentage of mislabeled pixels* (P_{mp}). (Cao & Newman, 2009). P_d is a summative measure of the distance variation between the extracted boundaries and the annotated auroral boundaries. P_g measures the gaps of the extracted equatorward boundary. P_f is the percentage of pixels that are far from the annotated auroral boundaries. P_{mp} indicates how much the extracted auroral oval region varies from the auroral oval region in the mask images. The smaller the values of these four metrics, the better the extracted boundaries. The performance of different methods is evaluated with the mean value and standard deviation of these metrics; the results are reported in Table3, in which the best metrics are labeled in bold.

Benefit from the distance constraint, as seen from Table 3, LIDLSM and the proposed method can effectively extract the complete auroral boundaries in the low-contrast regions, which are verified by the lower values of $M(P_g)$. Compared with LIDLSM, the proposed method owns the same mean value and higher standard deviation of P_g, partly because LIDLSM lowers the accuracy of the extracted boundaries to ensure the contour completeness of the auroral oval in the low-contrast regions, as shown in Figure 7d. FCM+QEF can extract an approximate contour of the auroral oval; however, it has relatively high values of these four metrics, especially when the poleward boundaries are rugged, which indicates that it cannot capture the local details of the boundaries.

Table 2. *The mean value $M(\cdot)$ and standard deviation $S(\cdot)$ of the four metrics using different methods on the test images.*

Methods	$M(P_d)$	$S(P_d)$	$M(P_g)$	$S(P_g)$	$M(P_f)$	$S(P_f)$	$M(P_{mp})$	$S(P_{mp})$
FCM+QEF	8.72	3.70	1.65	5.65	49.58	21.08	42.45	13.45
SIIALSM	8.97	12.54	1.24	2.91	25.76	33.56	34.91	23.61
LIDLSM	4.82	6.29	**0.57**	**1.91**	17.86	28.59	26.24	16.76
Proposed	**2.30**	**1.25**	**0.57**	2.33	**5.91**	**8.30**	**18.52**	**6.49**

4.2 Comparing with the SSJ Precipitation Boundary points

In order to further evaluate the accuracy of our algorithm, the extracted boundaries are projected onto the grid of magnetic local time (MLT) and magnetic latitude (MLAT) with the altitude-adjusted corrected geomagnetic coordinates (AAGCM) (Baker & Wing, 1989). Then the projected boundaries are matched and compared with the SSJ precipitation boundary points including b1e, b1i, b2e, b2i, b5e, b5i, and b6, which are determined using a set of quantitative algorithms proposed by Newell et al. (Newell et al., 1996) based on the in-situ precipitating particle data observed by DMSP/SSJ instruments. The matching condition is set that the observation time (T) difference between the Polar and DMSP satellites is less than three minutes (Carbary & J., 2003). Examples of the four matching results are shown in Figure 8, in which the different color lines denote the poleward boundaries (pol_b) and equatorward boundaries (equ_b) annotated by experts and extracted by our method. The different marks specify various SSJ precipitation boundary dots determined by the precipitating particle flux, and the different colors of the marks represent the source of the precipitating particle data. The red represents data from DMSP/F10 satellite, pink from the DMSP/F11 satellite, orange from the DMSP/F12 satellite. Clearly, in most regions, the extracted boundaries of the proposed method are consistent well with the annotated results. In addition, the equatorward boundaries are in good agreement with the precipitation boundary points. For the poleward boundaries, b1e is more consistent with the extracted contours than b1i, which is mainly because the auroral radiance in the LBHL wavelength originates from $\mathrm{N_2}$ emissions excited by the electron impact (Carbary & J., 2003).

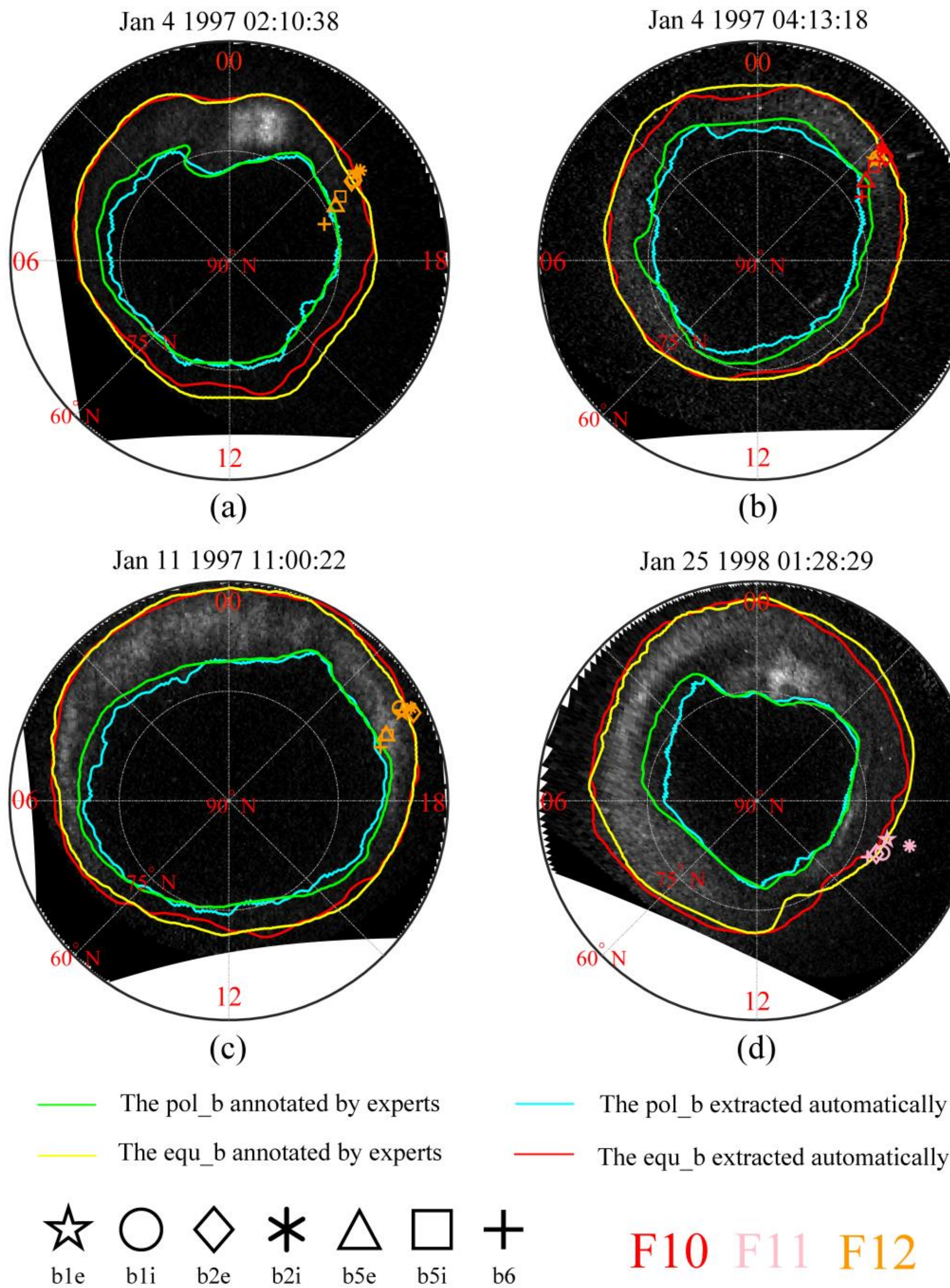

Figure 8. The matching results of auroral contours extracted from Polar/UVI images and boundary points determined by DMSP/SSJ precipitating particle data. The green and yellow lines denote the poleward boundaries (pol_b) and equatorward boundaries (equ_b) annotated by experts, and the blue and red lines indicate the pol_b and equ_b extracted by our method. The different marks specify various SSJ precipitation boundary dots determined by the precipitating particle flux, and the different colors of the marks represent the source of the precipitating particle data. Red represents data from DMSP/F10 satellite, pink from the DMSP/F11 satellite, orange from the DMSP/F12 satellite. (a) The UVI image captured at Jan 4, 1997, 02:10:38. (b) The UVI image captured at Jan 4, 1997, 04:13:18. (c) The UVI image captured at Jan 11, 1997, 11:00:22. (c) The UVI image captured at Jan 25, 1998, 01:28:29.

Since the auroral radiance observed by UVI LBHL wavelength is excited by precipitating electrons, we quantitatively compare the extracted equatorward and poleward boundaries with the precipitation boundaries b1e and b5e, respectively. According to the condition of $|T_{SSJ} - T_{UVI}| \leq 3\text{min}$ as above-mentioned, there are 28 equatorial matches and 29 poleward matches (57 total) in the 300 test UVI images. For each pair of matching boundaries, we calculate the offset between them. The calculation process is as follows:

1. Project the extracted UVI auroral boundary and SSJ precipitation boundary point onto the AAGCM. As shown in Figure 8, the extracted boundary is a complete contour which shows the global view of the auroral oval, while the DMSP/SSJ detector can only obtain isolated boundary points.
2. For a given SSJ precipitation boundary point, we find the corresponding point in the extracted UVI contour which has the same MLT, i.e., $MLT_{SSJ} = MLT_{UVI}$.
3. Calculate the MLAT difference between these two matching points ($MLAT_{SSJ} - MLAT_{UVI}$).

The MLAT difference is employed to evaluate the offset between the extracted boundaries and the SSJ precipitation boundary points, and the frequency histogram of the difference is shown in Figure 9, in which the different colors indicate the MLAT difference of equatorward and poleward boundaries, respectively.

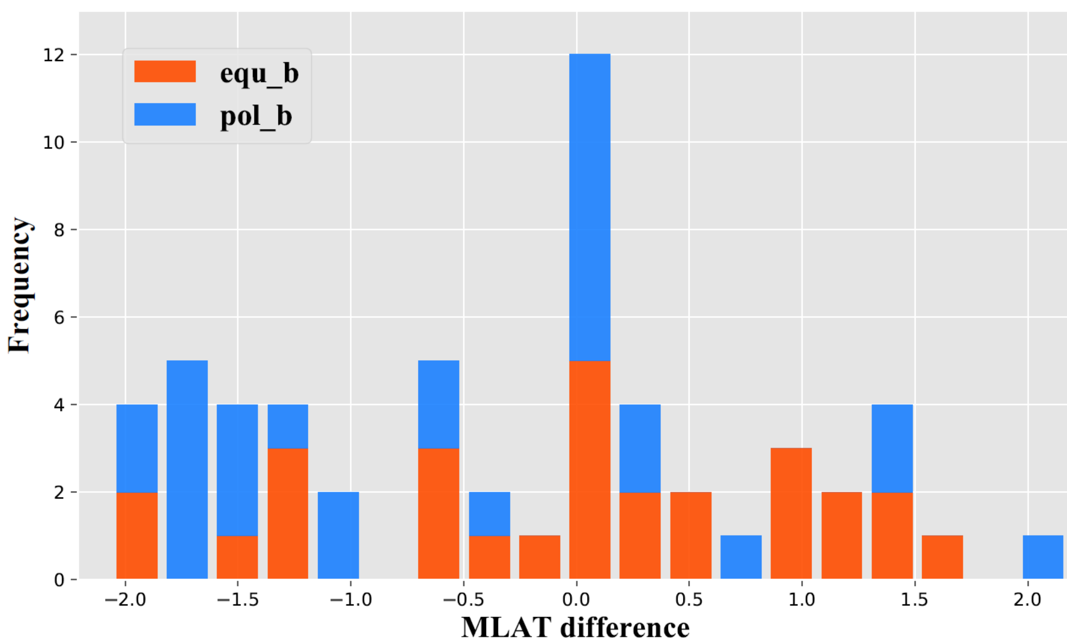

Figure 9. The frequency distribution histogram of MLAT difference.

As Figure 9 shows, the MLAT difference frequency of poleward and equatorward boundaries both reaches the maximum values at 0° , which reflects that, in most cases, the extracted boundaries conform well with the SSJ precipitation boundary points. The MLAT difference of equatorward boundaries is evenly distributed on the positive and negative semi-axis, and approximately follows the Gaussian distribution, so it is expected that there is no obvious systematic deviation between them. However, for the poleward boundaries, the MLAT difference is mainly distributed on the negative semi-axis. It indicates that the extracted poleward boundaries usually locate inside (closer to the geomagnetic pole) of the SSJ precipitation poleward boundary points, as shown in Figure 8a-c. In general, the MLAT difference between the extracted UVI auroral boundaries and the SSJ precipitation boundary points is within 2.2°, which demonstrates that the proposed auroral boundaries determination algorithm is reliable to capture the global configuration of the auroral ovals.

5 Conclusions

In this paper, based on the convolutional neural network and dual level set method, a new algorithm is proposed to extract the poleward and equatorward boundaries from the UVI images captured by NASA Polar satellite. With the confidence value derived from CNN, a deep feature energy term is devised and introduced into the level set framework. Attributing to the excellent performance of CNN, the advantages of the algorithm proposed in this investigation are as follows:

1. Compared with FCM+QEF, our algorithm retains the details of poleward and equatorward boundaries, which can help to uncover the physical mechanism of the solar wind-magnetosphere-ionosphere coupling process.
2. In the low-contrast regions of UVI images, SIIALSM cannot attain complete auroral oval. Though boundary leakage is prevented in the results of LIDLSM, the extracted boundaries deviate obviously from the annotated contours in those regions. In comparison with LIDLSM, the proposed algorithm not only extracts the complete auroral oval but also captures the local variation details in the low-contrast regions.
3. The comparison between the extracted UVI auroral boundaries with the SSJ precipitation boundary points in the test data set shows that the magnetic latitude difference between them is less than 2.2°. It demonstrates that the proposed algorithm is dependable to construct the auroral configuration from UVI images.

The proposed method can serve as a practical tool to locate the region and extract the global morphology of the auroral oval from UVI images. The accurate auroral boundaries can be used to model the relationship between the morphology of the auroral oval and the interplanetary or geomagnetic magnetospheric dynamic parameters. We notice that there exist incomplete auroral ovals in the UVI images, and for this circumstance, it is necessary to introduce the prior knowledge into the dual level set model to extract the complete auroral boundaries, which are our future directions.

Acknowledgments

This work was supported by the National Natural Science Foundation of China under Grant numbers 61473310, 41174164, 41775027, and 41904139. We would like to thank NASA's Space Physics Data Facility for providing Ultraviolet Imager (UVI) images which is available at https://cdaweb.gsfc.nasa.gov/index.html/ as well as the Johns Hopkins University Applied Physics Laboratory for providing the nightside SSJ boundary identifications data available at http://sd-www.jhuapl.edu/Aurora/dataset_list.html. Besides, the authors would like to thank Prof. Qinghe Zhang (Institute of Space Sciences, Shandong University) for his helpful guidance on our work. The code for extracting the confidence map can be downloaded at https://github.com/shuaichentian/Auroral-Boundary-Determination, and the boundary determination code will be uploaded to this website after the work is published. The pre-trained

CNN is available under https://github.com/shuaichentian/Auroral-Boundary-Determination/tree/master/Pre-trained%20CNN_PYTHON.

References

Akasofu, S. I. (1965). Dynamic morphology of auroras. *Space Science Reviews, 4*(4), 498-540. doi:10.1007/BF00177092.

Baker, K. B., & Wing, S. (1989). A new magnetic coordinate system for conjugate studies at high latitudes. *Journal of Geophysical Research, 94*, 9139. doi:10.1029/ja094ia07p09139.

Boudouridis, A., Zesta, E., Lyons, L. R., Anderson, P. C., & Lummerzheim, D. (2005). Enhanced solar wind geoeffectiveness after a sudden increase in dynamic pressure during southward IMF orientation. *Journal of Geophysical Research: Space Physics, 110*(A5). doi:10.1029/2004ja010704.

Boudouridis, A., Zesta, E., Lyons, R., Anderson, P. C., & Lummerzheim, D. (2003). Effect of solar wind pressure pulses on the size and strength of the auroral oval. *Journal of Geophysical Research: Space Physics, 108*(A4). doi:10.1029/2002ja009373.

Brittnacher, M., Spann, J., Parks, G., & Germany, G. (1997). Auroral observations by the polar Ultraviolet Imager (UVI). *Advances in Space Research, 20*(4), 1037-1042. doi:10.1016/S0273-1177(97)00558-9.

Cao, C., & Newman, T. S. (2009). New shape-based auroral oval segmentation driven by LLS-RHT. *Pattern Recognition, 42*(5), 607-618. doi:10.1016/j.patcog.2008.08.018.

Carbary, & J., F. (2003). Auroral boundary correlations between UVI and DMSP. *Journal of Geophysical Research, 108*(A1), 1018. doi:10.1029/2002ja009378.

Clausen, L. B. N., & Nickisch, H. (2018). Automatic Classification of Auroral Images From the Oslo Auroral THEMIS (OATH) Data Set Using Machine Learning. *Journal of Geophysical Research: Space Physics, 123*(7), 5640-5647. doi:10.1029/2018ja025274.

de Boer, P.-T., Kroese, D. P., Mannor, S., & Rubinstein, R. Y. (2005). A Tutorial on the Cross-Entropy Method. *Annals of Operations Research, 134*(1), 19-67. doi:10.1007/s10479-005-5724-z.

Ding, G.-X., He, F., Zhang, X.-X., & Chen, B. (2017). A new auroral boundary determination algorithm based on observations from TIMED/GUVI and DMSP/SSUSI. *Journal of Geophysical Research: Space Physics, 122*(2), 2162-2173. doi:10.1002/2016ja023295.

Drożdż, M., & Kryjak, T. (2017). FPGA Implementation of Multi-scale Face Detection Using HOG Features and SVM Classifier. *Image Processing & Communications, 21*, 27-44. doi:10.1515/ipc-2016-0014.

Fei, Z., & Zhang, J. S. (2011). *Softmax Discriminant Classifier.* Paper presented at the International Conference on Multimedia Information Networking & Security.

Girshick, R. (2015). *Fast R-CNN.* Paper presented at the IEEE International Conference on Computer Vision.

Goodfellow, I. J., Pouget-Abadie, J., Mirza, M., Bing, X., Warde-Farley, D., Ozair, S., et al. (2014). *Generative Adversarial Nets.* Paper presented at the International Conference on Neural Information Processing Systems.

Ham, Y.-G., Kim, J.-H., & Luo, J.-J. (2019). Deep learning for multi-year ENSO forecasts. *Nature, 573*(7775), 568-572. doi:10.1038/s41586-019-1559-7.

Hoffman, R. A., & Hesse, M. (1996). *Global Geospace Science (GGS) Program and the Polar Satellite.* Paper presented at the International Conference on Substorms.

Hoshi, Y., Hasegawa, H., Kitamura, N., Saito, Y., & Angelopoulos, V. (2018). Seasonal and Solar Wind Control of the Reconnection Line Location on the Earth's Dayside Magnetopause. *Journal of Geophysical Research: Space Physics, 123*(9), 7498-7512. doi:10.1029/2018ja025305.

Hu, Z.-J., Yang, Q.-J., Liang, J.-M., Hu, H.-Q., Zhang, B.-C., & Yang, H.-G. (2017). Variation and modeling of ultraviolet auroral oval boundaries associated with interplanetary and geomagnetic parameters. *Space Weather, 15*(4), 606-622. doi:10.1002/2016sw001530.

Kass, M., Witkin, A., & Terzopoulos, D. (1988). Snakes: Active contour models. *International Journal of Computer Vision, 1*(4), 321-331. doi:10.1007/bf00133570.

Kauristie, K., Weygand, J., Pulkkinen, T. I., Murphree, J. S., & Newell, P. T. (1999). Size of the auroral oval: UV ovals and precipitation boundaries compared. *Journal of Geophysical Research, 104*(A2), 2321. doi:10.1029/1998ja900046.

Kvammen, A., Gustavsson, B., Sergienko, T., Brändström, U., Rietveld, M., Rexer, T., & Vierinen, J. (2019). The 3-D Distribution of Artificial Aurora Induced by HF Radio Waves in the Ionosphere. *Journal of Geophysical Research: Space Physics, 124*(4), 2992-3006. doi:10.1029/2018ja025988.

Liu, H., Gao, X., Han, B., & Yang, X. (2013, 31 July - 2 August). *An Automatic MSRM Method with a Feedback Based on Shape Information for Auroral Oval Segmentation.* Paper presented at the international conference on intelligent science and big data engineering, Beijing.

Meng, Y., Zhou, Z., Liu, Y., Luo, Q., Yang, P., & Li, M. (2019). A prior shape-based level-set method for auroral oval segmentation. *Remote Sensing Letters, 10*(3), 292-301. doi:10.1080/2150704x.2018.1547928.

Nair, V., & Hinton, G. E. (2010). *Rectified Linear Units Improve Restricted Boltzmann Machines.* Paper presented at the International Conference on International Conference on Machine Learning.

Newell, P. T., Feldstein, Y. I., Galperin, Y. I., & Meng, C.-I. (1996). Morphology of nightside precipitation. *Journal of Geophysical Research: Space Physics, 101*(A5), 10737-10748. doi:10.1029/95ja03516.

Niu, C., Yang, Q., Ren, S., Hu, H., Han, D., Hu, Z., & Liang, J. (2019). Instance Segmentation of Auroral Images for Automatic Computation of Arc Width. *IEEE Geoscience and Remote Sensing Letters*, *16*(9), 1-5. doi:10.1109/lgrs.2019.2901803.

Phung, & Rhee. (2019). A High-Accuracy Model Average Ensemble of Convolutional Neural Networks for Classification of Cloud Image Patches on Small Datasets. *Applied Sciences*, *9*, 4500. doi:10.3390/app9214500.

Qian, W., QingHu, M., ZeJun, H., ZanYang, X., JiMin, L., & HongQiao, H. (2011). Extraction of auroral oval boundaries from UVI images: A new FLICM clustering-based method and its evaluation. *Advances in Polar Science*, *22*(3), 184-191. doi:10.3724/SP.J.1085.2011.00184.

Redmon, R. J., Denig, W. F., Kilcommons, L. M., & Knipp, D. J. (2017). New DMSP database of precipitating auroral electrons and ions. *Journal of Geophysical Research: Space Physics, 122*(8), 9056-9067. doi:10.1002/2016ja023339.

Schumaker, T., Hardy, D., Moran, S., Huber, A., & McGarity, J. (1988). Precipitating Ion and Electron Detectors (SSJ/4) for the Block 5D/Flight 8 DMSP (Defense Meteorological Satellite Program) Satellite. Air Force Geophys. Lab., Hanscom Air Force Base, Bedford, Mass., 61.

Shi, J., Wu, J., Anisetti, M., Damiani, E., & Jeon, G. (2017). An interval type-2 fuzzy active contour model for auroral oval segmentation. *Soft Computing, 21*(9), 2325-2345. doi:10.1007/s00500-015-1943-7.

Silver, D., Schrittwieser, J., Simonyan, K., Antonoglou, I., Huang, A., Guez, A., et al. (2017). Mastering the game of Go without human knowledge. *Nature, 550*, 354. doi:10.1038/nature24270.

Srivastava, N., Hinton, G., Krizhevsky, A., Sutskever, I., & Salakhutdinov, R. (2014). Dropout: a simple way to prevent neural networks from overfitting. *The Journal of Machine Learning Research*, *15*, 1929–1958.

Sun, L., Meng, X., Xu, J., & Zhang, S. (2018). An Image Segmentation Method Based on Improved Regularized Level Set Model. *Applied Sciences, 8*, 2393. doi:10.3390/app8122393.

Torr, M. R., Torr, D. G., Zukic, M., Johnson, R. B., Ajello, J., Banks, P., et al. (1995). A far ultraviolet imager for the International Solar-Terrestrial Physics Mission. *Space Science Reviews, 71*(1), 329-383. doi:10.1007/BF00751335.

Woo, J., Slomka, P. J., Kuo, C. C. J., & Hong, B. (2013). Multiphase segmentation using an implicit dual shape prior: Application to detection of left ventricle in cardiac MRI. *Computer Vision and Image Understanding, 117*(9), 1084-1094. doi:10.1016/j.cviu.2012.11.012.

Yang, P., Zhou, Z., Shi, H., & Meng, Y. (2017). Auroral oval segmentation using dual level set based on local information. *Remote Sensing Letters*, *8*(12), 1112-1121. doi:10.1080/2150704X.2017.1354260.

Yang, Q., Tao, D., Han, D., & Liang, J. (2019). Extracting Auroral Key Local Structures From All-Sky Auroral Images by Artificial Intelligence Technique. *Journal of Geophysical Research: Space Physics*, *124*(5), 3512-3521. doi:10.1029/2018ja026119.

Yang, X., Gao, X., Li, J., & Han, B. (2014a). A shape-initialized and intensity-adaptive level set method for auroral oval segmentation. *Information Sciences, 277*, 794-807. doi:10.1016/j.ins.2014.03.014.

Yang, X., Gao, X., Tao, D., & Li, X. (2014b). Improving Level Set Method for Fast Auroral Oval Segmentation. *IEEE Transactions on Image Processing, 23*(7), 2854-2865. doi:10.1109/TIP.2014.2321506.

Zhao, H., Shi, J., Qi, X., Wang, X., & Jia, J. (2017). *Pyramid Scene Parsing Network.* Paper presented at the IEEE Conference on Computer Vision & Pattern Recognition.

Figure 1. Overview of the proposed auroral oval boundaries determination method.

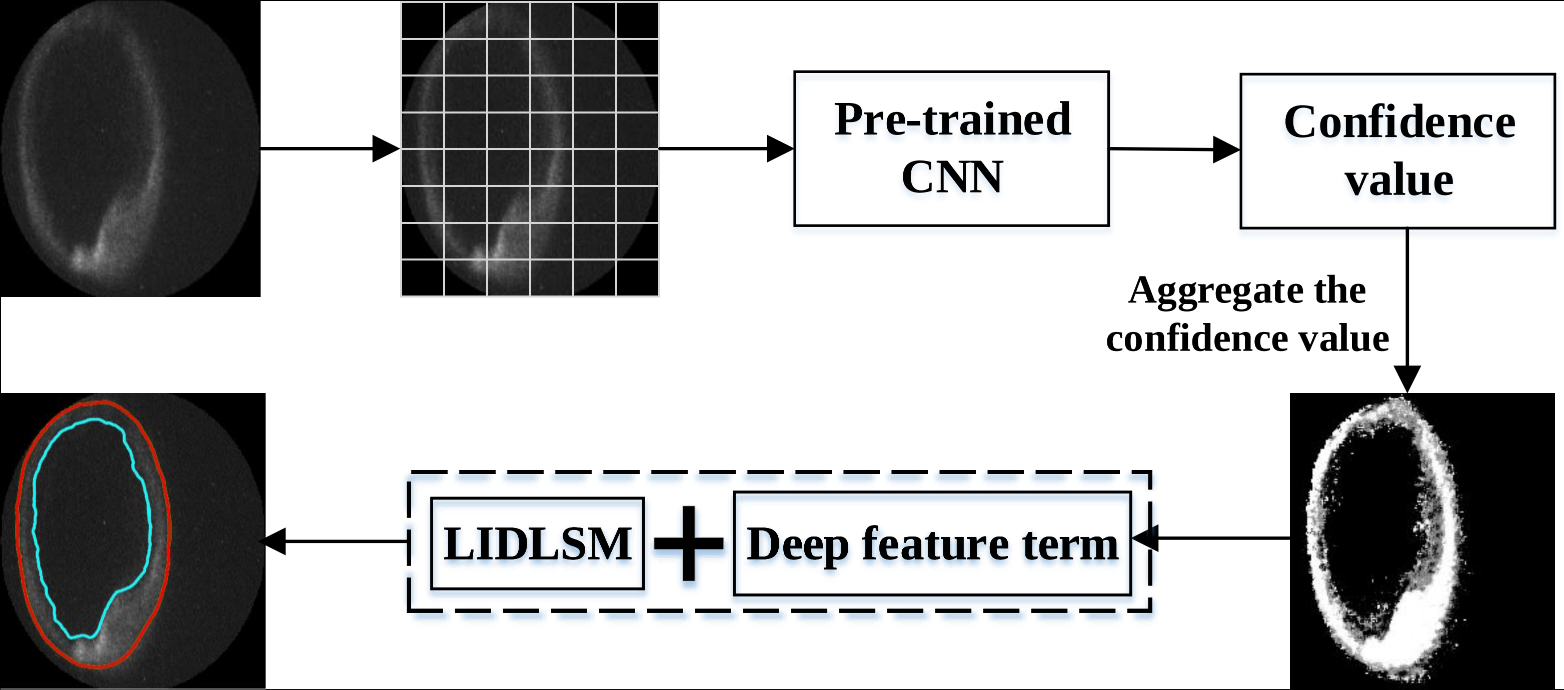

Pre-trained CNN
Confidence value
Aggregate the confidence value
LIDLSM
Deep feature term

Figure 2. UVI data set images: (a) the auroral image captured at Jan 1, 1997, 02:28:43; (b) the annotated auroral boundary image; (c) the corresponding mask image.

(a) (b) (c)

Figure 3. UVI image and extracted boundaries. (a) The UVI image captured at Jan 10, 1997, 03:40:12. (b) Extracted boundaries by LIDLSM. (c) Annotated boundaries by experts..

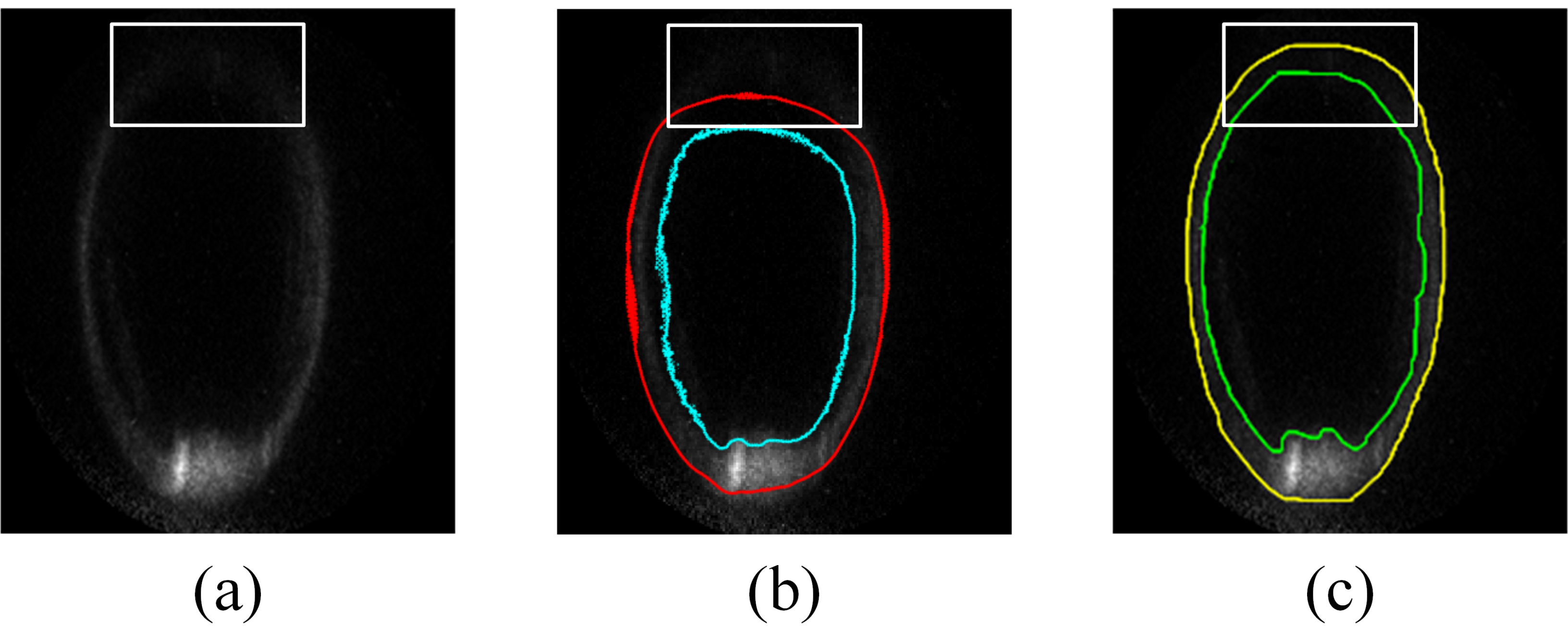
(a)
(b)
(c)

Figure 4. The extraction procedure of training samples and labels.

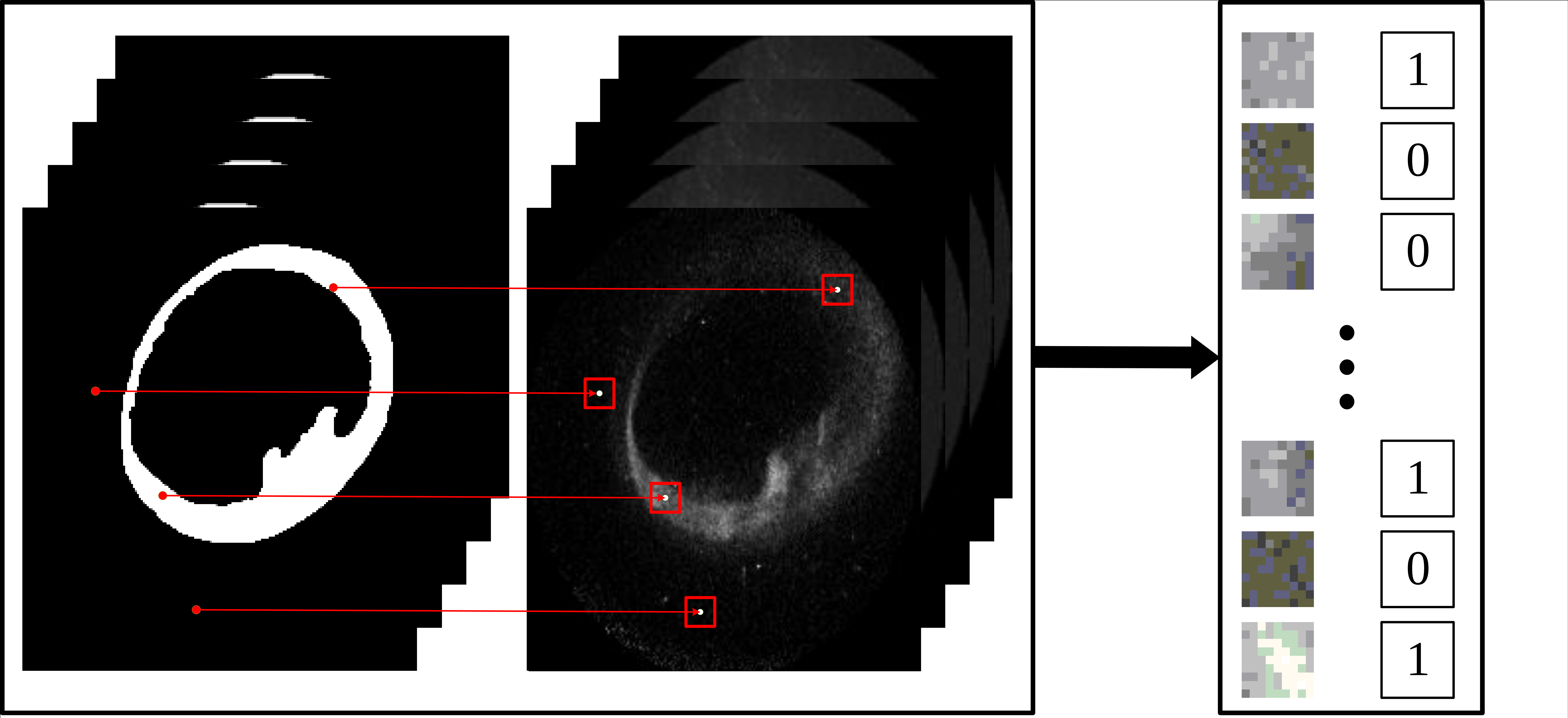

50 pairs of auroral oval images and mask images

200000 pairs of training samples and labels

Figure 5. Comparison of UVI image and corresponding confidence map. (a) UVI image captured at Jan 10, 1997, 03:40:12. (b). Corresponding confidence map.

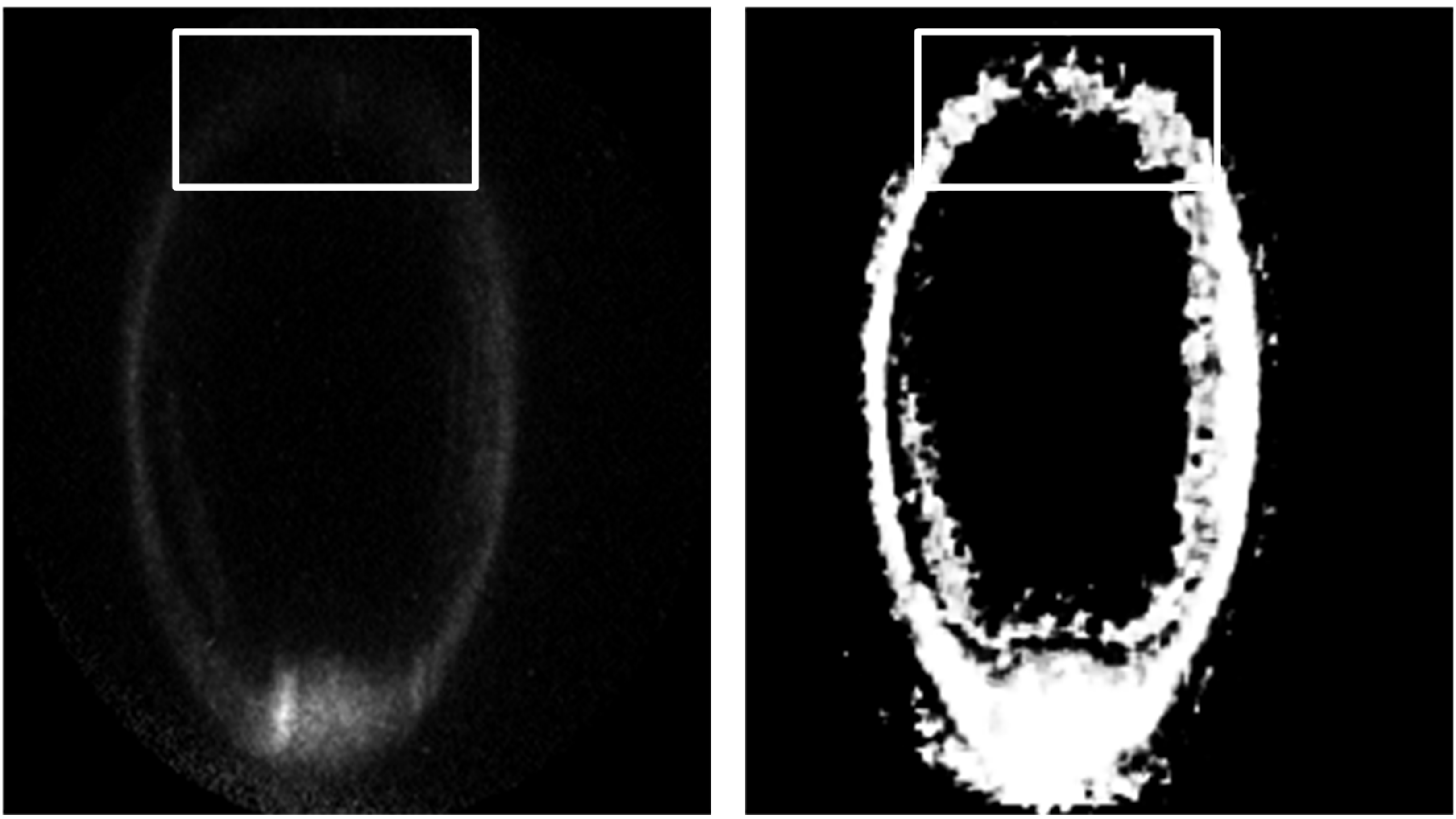

(a) (b)

Figure 6. Segmentation result of our method.

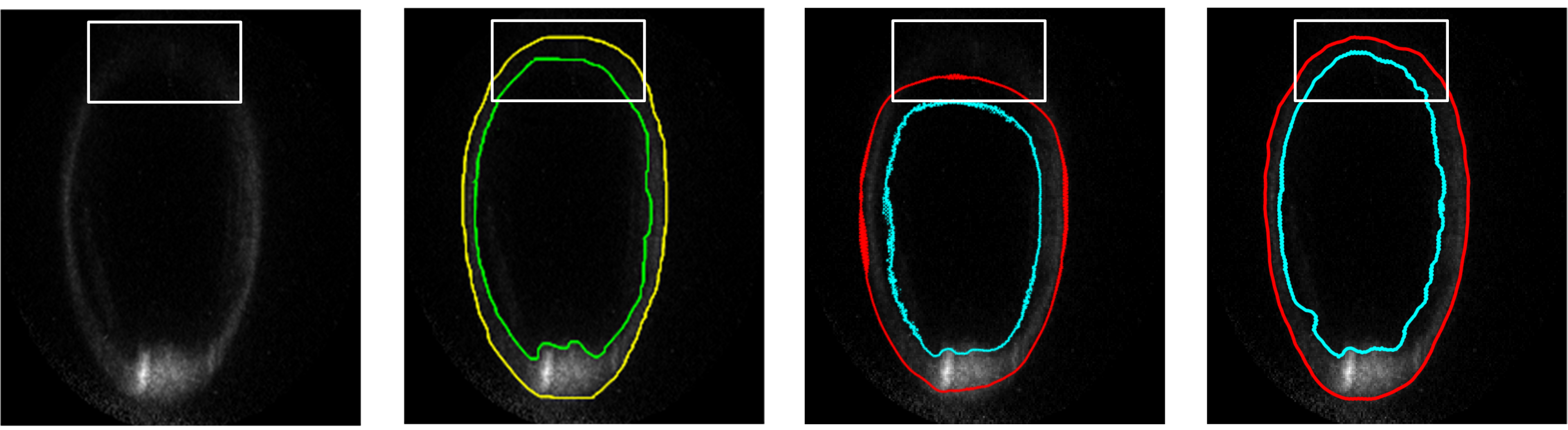

(a) (b) (c) (d)

Figure 7. The UVI images, the mask images, and the auroral oval region extracted by different methods.

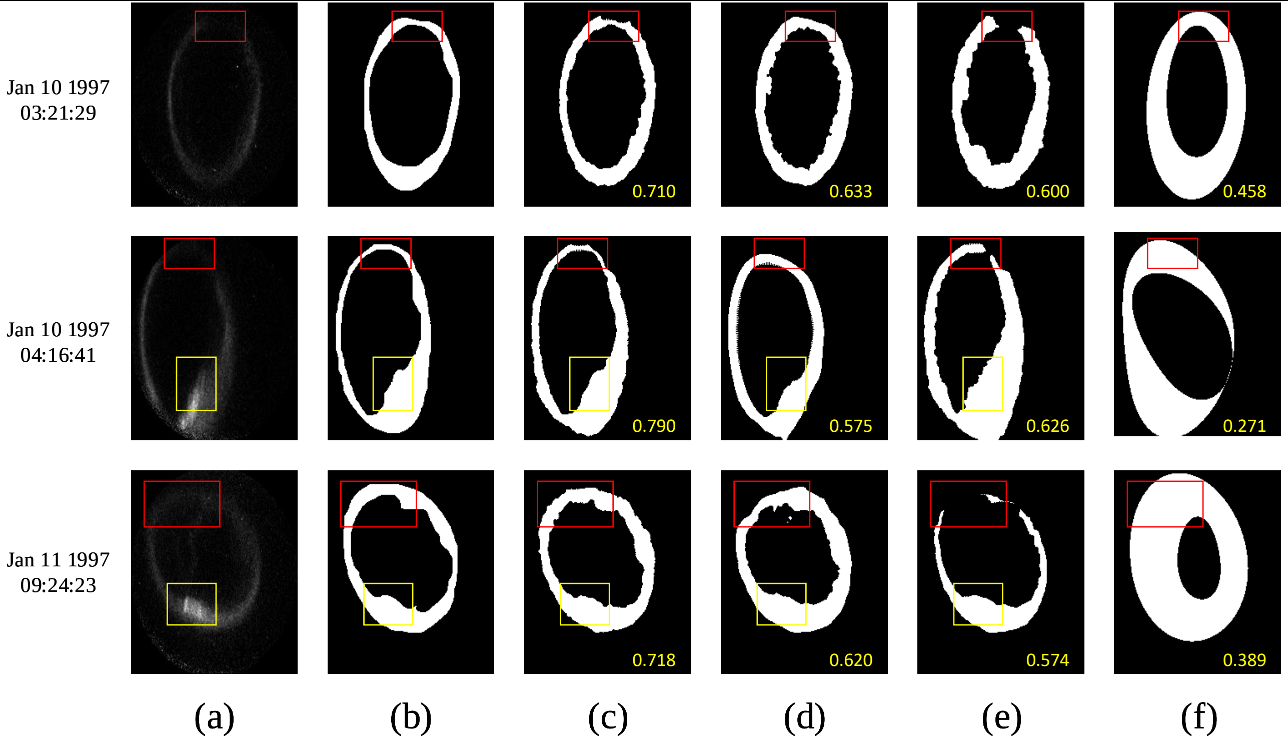
Jan 10 1997
03:21:29
0.710
0.633
0.600
0.458
Jan 10 1997
04:16:41
0.790
0.575
0.626
0.271
Jan 11 1997
09:24:23
0.718
0.620
0.574
0.389
(a)
(b)
(c)
(d)
(e)
(f)

Figure 8. The matching results of auroral contours extracted from Polar/UVI images and boundary points determined by DMSP/SSJ precipitating particle data.

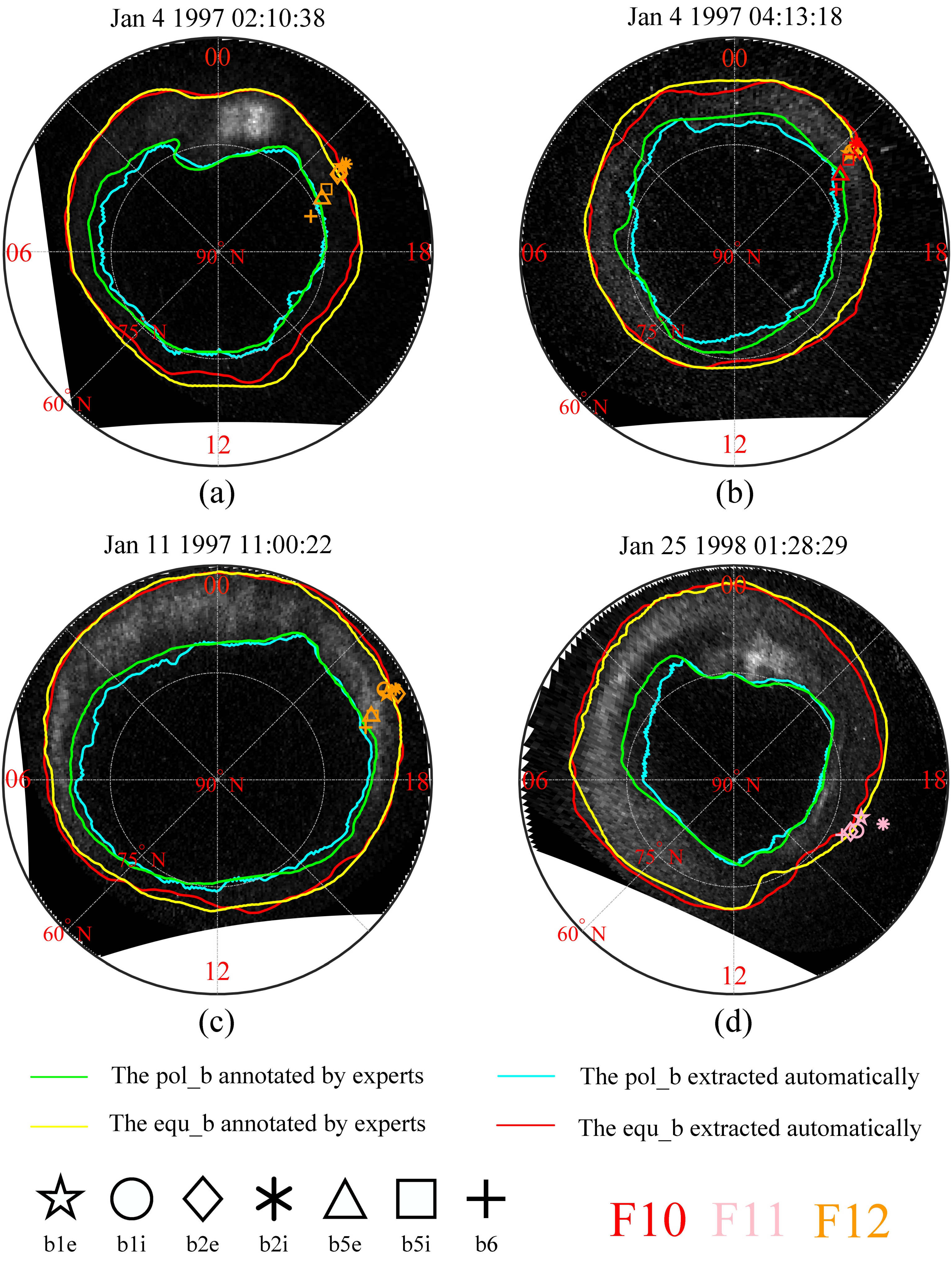
Jan 4 1997 02:10:38
Jan 4 1997 04:13:18
Jan 11 1997 11:00:22
Jan 25 1998 01:28:29
00
06
18
12
90° N
75° N
60° N
(a)
(b)
(c)
(d)
The pol_b annotated by experts
The pol_b extracted automatically
The equ_b annotated by experts
The equ_b extracted automatically
b1e
b1i
b2e
b2i
b5e
b5i
b6
F10
F11
F12

Figure 9. The frequency distribution histogram of MLAT difference.

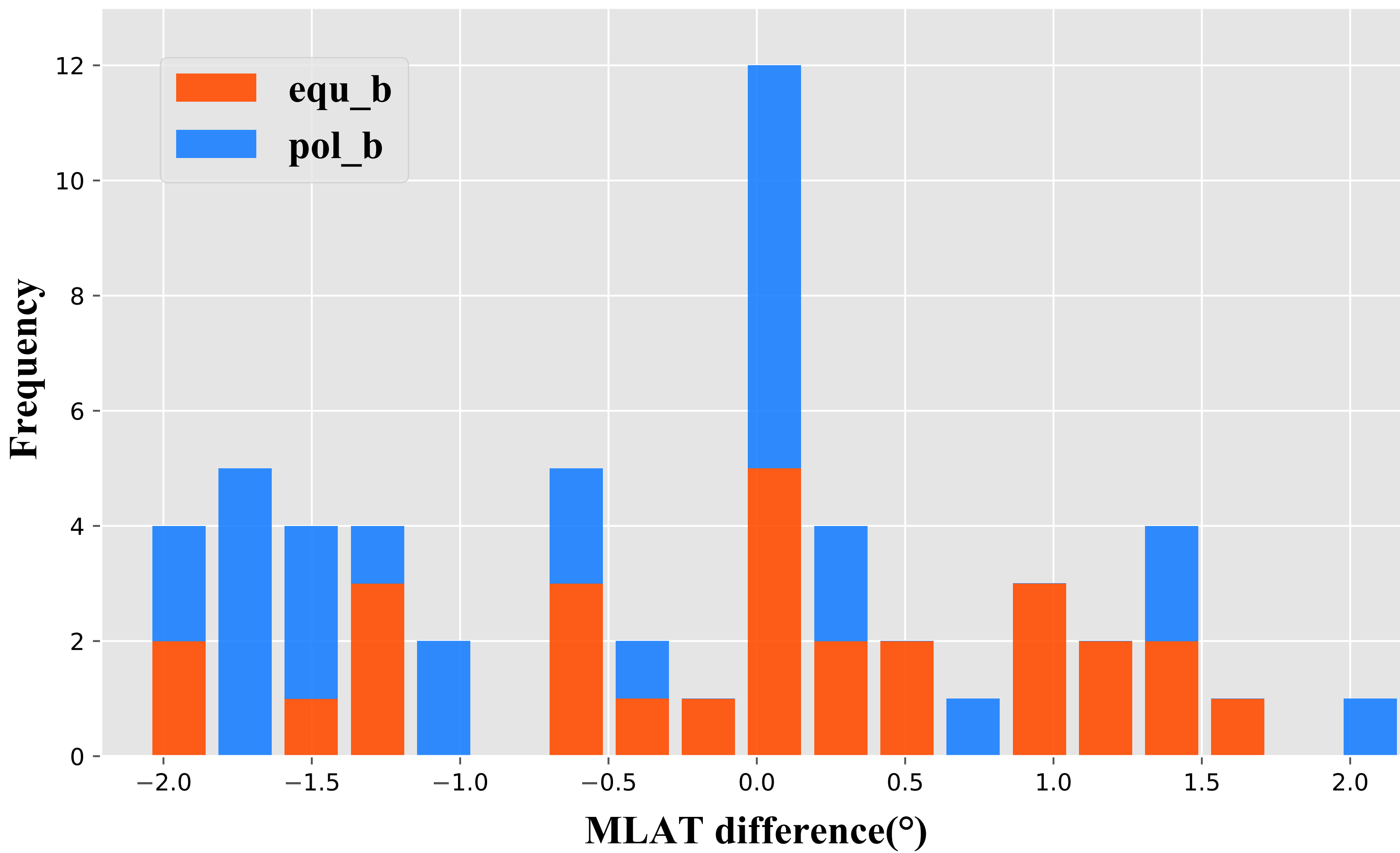

equ_b
pol_b
Frequency
MLAT difference(°)
0
2
4
6
8
10
12
−2.0
−1.5
−1.0
−0.5
0.0
0.5
1.0
1.5
2.0